Nitrogen Doped Porous Carbons Derived from Walnut Shell as an Oxygen Reduction Catalyst for Mg-Air Batteries

[1]Kun Liu, [1]Fanqing Ji, [1]Guangyue Zhou, [1]Jing Wang, [1]Haoyi Li, [1]Xiuxian Quan, [1]Angli Zhang, [1]Kaiqi Liu, [2]Xucheng Fu* and [1]Xiaowu Liu[a]*

[1] Anhui Province Key Laboratory of Conservation and Utilization for Dabie Mountain Special Bio-Resources, College of Materials and Chemical Engineering, West Anhui University, Lu'an 237012, Anhui Province, China.

[2]Analytical and Testing Center, West Anhui University, Lu'an 237012, Anhui Province, China.

708934891@qq.com*

(Received on 5th March 2025, accepted in revised form 21st October 2025)

Summary: The present study proposes a nitrogen-doped carbon material with an improved pore structure, facilitating efficient mass transfer and offering abundant active sites for electrocatalytic oxygen reduction. The present study successfully synthesized a series of N-doped carbons with three-dimensional interpenetrating layered porous structures by utilizing NaOH as a pore-forming agent during the carbonization process of biomass refuse. The half-wave potential of $NWSC_{0.6}$ (N-doped walnut shells carbon) ($E_{1/2}$ = 0.849 V) exceeds that of 20 wt% Pt/C by 9 mV. The catalyst exhibited exceptional catalytic performance and remarkable stability. The discharge voltage of the Mg-air battery utilizing $NWSC_{0.6}$ as the cathode catalyst consistently outperforms that of the battery employing 20% wt% Pt/C as the cathode catalyst. The synthesis of noble-metal-free catalysts derived from natural biological resources exhibits superior electrochemical performance in Mg-air batteries.

Keywords: Magnesium-air batteries, Catalysts, Oxygen reduction reaction, non-precious metal, porous structures.

Introduction

The escalating energy crisis and environmental pollution resulting from excessive dependence on fossil fuels have sparked significant interest in the development of cost-effective, high-efficiency, environmentally-friendly, and sustainable energy conversion and storage systems.[1-3] The fuel cell, being the primary energy conversion device in the future, has garnered significant attention from researchers due to its notable advantages including high energy output, rapid transmission speed, environmental friendliness, and ease of operation.[4-6] The cathodic oxygen reduction in fuel cells proceeds at a sluggish rate, necessitating the use of catalysts. Among these, Pt-based precious metal catalysts (such as Pt/C) have been identified as the most efficient catalysts for ORR.[7-9] The utilization of Pt-based catalysts in large-scale commercial applications is restricted due to their high cost, sluggish cathode reaction kinetics, and long-term instability.[10] To address the limitations of Pt-based catalysts and further advance the widespread implementation of fuel cells, it is imperative to urgently develop novel ORR catalysts that exhibit reduced cost, enhanced activity, and superior stability.[11] To date, the quest for cost-effective non-metallic catalysts that can achieve high performance levels comparable to or surpassing those of commercial Pt/C has garnered significant attention from researchers.[12] Non-metal heteroatom-doped carbon materials possess the advantages of cost-effectiveness, tunable pore structure, high conductivity, and excellent impurity tolerance, rendering them highly promising for applications in the field of ORR catalysts.[13, 14] Among these materials, non-metallic catalysts are widely regarded as the most viable alternatives to platinum-based catalysts.[15]

The walnut shell is a plentiful biomass waste on earth, characterized by its ease of extraction and low cost. Comprising primarily cellulose (30.88% of total content), hemicellulose (27.26% of total content), and lignin (38.05% of total content), it exhibits a layered porous structure at the microscopic level.[16, 17] Additionally, the annual cultivation of a substantial quantity of walnuts in the Anhui province section of the Dabie Mountain area results in the generation of walnut shell waste, imposing a significant societal burden and energy wastage. The carbon nanostructures formed by high temperature carbonization activation of biomass waste are characterized by well-developed internal pores, a high surface area, excellent electrical conductivity, and corrosion resistance.[18] The biological source carbon

*To whom all correspondence should be addressed.

serves as a highly efficient carrier catalyst for ORR, enabling uniform integration with non-metallic atoms to generate numerous active sites.[19] This renders it an ideal material for fuel cell catalysts.[20] The high carbon content, low cost, non-toxicity, and environmental friendliness of biomass waste make it a widely applicable raw material for the production of activated carbon.

The incorporation of nitrogen atoms into the carbon structure induces structural distortion, alters charge density, and modifies the electronic structure of carbon materials, consequently influencing their adsorption free energy towards reactants and intermediates.[21, 22] This ultimately impacts the ORR performance of nitrogen-doped carbon-based catalysts. Nitrogen serves as an essential source in the preparation of these catalysts and can act as active sites.[23, 24] In the previous research work, the primary raw materials were predominantly artificially synthesized chemical reagents. Two specific preparation schemes were employed: first, maltose was utilized as the carbon source, supplemented with $CuCl_2 \cdot 2H_2O$ and $FeCl_3 \cdot 4H_2O$ as dual metal sources, and dicyandiamide as the nitrogen source; [25] second, sucrose served as the carbon source, urea as the nitrogen source, and Fe/Co compounds as the metal sources.[26] Both approaches employed NaCl as a hard template to construct porous architectures. However, these methods shared several limitations: the first required multiple processing steps, including freeze-drying, grinding, molten-salt pyrolysis under sealed conditions, and extensive water washing for template removal; although the second also relied on NaCl templating, it similarly necessitated post-synthesis treatments for template elimination. These procedures not only rendered the synthesis process complex and time-consuming but also increased production costs due to water consumption and generated significant wastewater, posing environmental challenges. To address these challenges, this study proposes a transition from conventional designs based on metal active sites to a regulatory strategy focused on the intrinsic structure and elemental composition of biomass, thereby enabling substantial innovation in the synthetic methodology.

The present study involves the preparation of a highly efficient porous catalyst for ORR through high temperature annealing, utilizing walnut shell as a precursor material for carbon. The NWSC (N-doped walnut shells carbon) material was prepared from walnut shells in the Dabie Mountain area through NaOH activation and urea nitrogen source doping. The NWSC material exhibits not only a significantly large specific surface area and abundant pores, but also possesses an abundance of carbon, nitrogen, and oxygen functionalities, which greatly enhances its electrocatalytic performance. The $NWSC_{0.6}$ catalysts demonstrate exceptional ORR catalytic performance in alkaline conditions (0.1 M KOH), thereby opening up new possibilities for the design of highly efficient multifunctional electrocatalysts for energy storage and conversion devices.

Experiment

Chemicals and materials

Urea (H_2NCONH_2, 99%, Aladdin), ethanol (C_2H_5OH, ≥99.9%, Macklin), sodium chloride (NaCl, 99%, Aladdin), sodium hydroxide (NaOH, 99%, Aladdin) and potassium hydroxide (KOH, 95%, Aladdin) were purchased individually. The 20 wt% Pt/C (Johnson Matthey) was procured from Hefei Aiyan Medical biological Co., LTD, China. Nitric acid (HNO_3, Xilong Technology) and Hydrochloric acid (HCl, 95%) are purchased through the unified government procurement process. Ketjenblack carbon (EC300J), and Acetylene black (Dedka Black Li-2060) were purchased from Saibo Electrochemical Materials Co., LTD, which is utilized without undergoing any additional purification treatment. Our laboratory procures the 5wt% Nafion solution from DuPont for use in our research. Walnut shells are derived from walnut trees planted in Dabie Mountain area. The industrial-grade magnesium alloy sheet, nickel foam, and waterproof breathable film are provided by Changzhou Youtec New Energy Technology Co., LTD.

Synthesis of porous carbon materials

The synthesis procedures are illustrated in Fig 1 and elaborated upon in detail below. The walnut shells were placed in a blast drying oven at 80 ℃ for 24 hours. Subsequently, the dried walnut shells were ground into powder and subjected to heating in a Muffle furnace at a rate of 5 $℃ \cdot min^{-1}$ from room temperature to 400 ℃, followed by a holding time of 2 hours. After cooling to room temperature, the samples were retrieved and further ground for subsequent use. We precisely weighed 1 g of the aforementioned pre-carbonized carbon, added 3 g of sodium hydroxide, and ground it thoroughly. Subsequently, we transferred the mixture to a

porcelain boat and subjected it to heating in a tube furnace under a nitrogen atmosphere at a rate of 5 ℃·min^{-1} from room temperature to 800 ℃. The sample was maintained at this temperature for one hour before being naturally cooled back to room temperature for subsequent grinding. The activated sample was placed in a 250 mL beaker, and approximately 200 mL of deionized water was added. Subsequently, concentrated nitric acid was gradually introduced into the solution until reaching a pH value of 1. The solution underwent magnetic stirring at room temperature for a duration of 8 hours. Following this, it was subjected to multiple rinses with deionized water until achieving neutrality before being drained and left to dry overnight. The resulting sample was then labeled as WSC (walnut shells carbon).

In order to further optimize and obtain carbon materials with excellent properties, the above 0.1 g of WSC was weighed and thoroughly ground with varying amounts of urea (0.4 g, 0.5 g, 0.6 g, and 0.7 g). The mixture was then placed in a tube furnace under a nitrogen atmosphere and heated from room temperature to 850 ℃ at a heating rate of 5 ℃·min^{-1} before being kept warm for 3 hours. After natural cooling to room temperature, the samples were removed and finely ground. These samples were subsequently labeled as $NWSC_{0.4}$, $NWSC_{0.5}$, $NWSC_{0.6}$, and $NWSC_{0.7}$.

Material characterization

The crystal morphology, phase composition, and microstructure of the materials were analyzed using a German D8 X-ray diffractometer (XRD) with cu-k-α radiation in the 2θ rotation range of 10°~80°. Additionally, the test requires an angular accuracy of 0.0001°, ensuring that the angular deviation of each peak within the entire spectral range does not exceed ±0.01 degrees. The distribution, morphology, and microscopic size of the powder samples were analyzed using a scanning electron microscope (Hitachi SU3500) and an energy dispersive spectrometer (EDS). The acceleration voltage range was set at 0.1 ~ 30 kV. Additionally, high-resolution transmission electron microscopy (TEM) with FEI-TALOS-F200X and an electron energy loss microspectrometer were employed to capture images of the samples. At West Anhui University of the Analysis and Testing Center, Raman spectroscopy is employed using a 532 nm laser source to detect chemical composition and the structure of the substance. The chemical composition and state of the samples were analyzed utilizing X-ray photoelectron spectroscopy (XPS) on an axial superDLD Kratos on-axis system with Al-Kα source. Furthermore, N_2 adsorption isotherm analysis was conducted using AUTOSORB IQ surface analyzer to measure the sample's surface area and pore diameter.

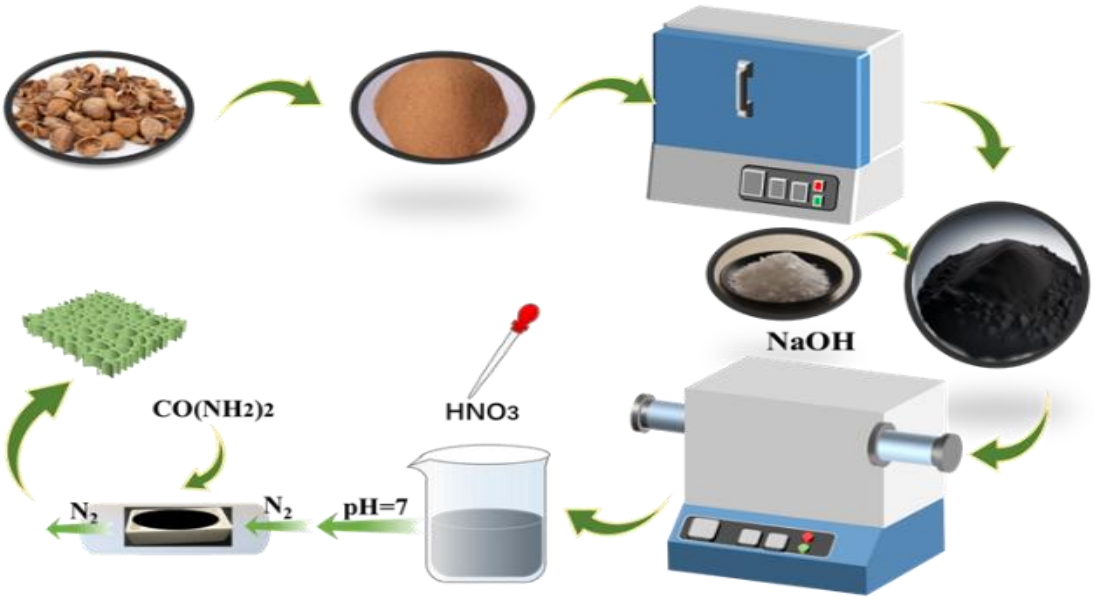

Fig. 1: Schematic of the synthesis procedure of $NWSC_x$ (x= 0.4, 0.5, 0.6 and 0.7).

Electrochemical measurements

The prepared catalyst series (4 mg) was dispersed in 950 μL of ethanol and subsequently added to a 100 μL solution of Nafion (5 wt%). Ultrasound was applied for a duration of 20 minutes to achieve a homogeneous suspension. The glassy carbon electrode, with a diameter of 5 mm, was uniformly coated with a mixture exceeding 10 μL to serve as the working electrode. This formed a three-electrode system in conjunction with the reference electrode [Hg/HgO (1 M KOH)] and the counter-electrode (A graphite rod). Prior to the electrochemical data collection, it is necessary to saturate the 0.1 M KOH solution with high-purity oxygen for 30 minutes to achieve a fully oxygen-saturated solution. The ORR characteristics of samples were investigated using a rotating ring electrode (RRDE) in a 0.1M O_2-saturated KOH solution at an electrochemical station manufactured by Ivium, the Netherlands. The experiments were conducted at room temperature with all electrochemical tests performed at a scan rate of 10 $mV \cdot s^{-1}$.The cyclic voltammetry (CV) curves were scanned at a consistent scanning rate within the voltage range of -1.0 ~ 0.2V. The NWSC catalyst was subjected to 2000 cycles of circulation in a 0.1 M O_2-saturated KOH solution, employing a scanning rate of 50 $mV \cdot s^{-1}$ and a potential range of 0.6 ~ 1.2 V.

The electron transfer number (n) was evaluated based on the Equations (S1, S2, S3†) in the electronic supplementary information (ESI).

Results and discussion

Structure and morphology characterization

The XRD patterns of the prepared WSC and $NWSC_{0.6}$ samples are depicted in Fig 2a, revealing a weak peak at approximately 43.7°, indicative of the presence of graphitized carbon.[23, 27] The diffraction peak of nitrogen is not observed due to its low detectable quantity, and the incorporation of nitrogen atoms into the carbon framework in a disordered manner forms the ORR active site of the carbon-based catalyst.[28] To further analyze the structure of the amorphous carbon materials prepared, Raman spectral analysis was conducted. Fig 2b displays the Raman spectrum of the sample within a range of 1000-2000 cm^{-1}. Two distinct peaks are identifiable, with the peak at 1334 cm^{-1} being associated with a defective disordered carbon structure (disordered sp^3 atoms), commonly referred to as the D-band. In addition, the peaks observed at 1602 cm^{-1} (corresponding to the G-band) primarily arise from the graphite structure, which consists of sp^2 hybridized carbon atoms arranged in a two-dimensional hexagonal lattice, or from the tensile motion of planar bonds between these sp^2 carbon atoms.[16, 29] Generally speaking, the ratio of D-band to G-band intensity (I_D/I_G) can be employed as an indicator for assessing the level of graphitization in carbon materials. The degree of graphitization is a crucial parameter that influences the electrical conductivity of carbon.[30] It can be observed from the I_D/I_G value that, in comparison to WSC (I_D/I_G=0.998), $NWSC_{0.6}$ exhibits significantly higher disorder in its carbon structure (I_D/I_G=1.013). This indicates an increased presence of defect sites in the carbon due to N doping. The introduction of N atoms leads to the generation of a plethora of defects, which contribute to the provision of potential active sites for ORR.[31] The presence of significant defects facilitates the reduction in ORR reaction barrier, thereby enhancing charge diffusion and overall reaction rate, ultimately improving electrochemical performance.[32] The specific surface area of WSC and $NWSC_{0.6}$ was determined using the nitrogen adsorption/desorption method, as illustrated in Fig S1. The specific surface area of WSC is measured to be 3121.9264 $m^2 \cdot g^{-1}$. The activation process with NaOH indicates the generation of abundant pore structure through strong chemical etching reaction between carbon atoms and NaOH, which has been further analyzed by SEM.[33] The specific surface area of $NWSC_{0.6}$ is 2636.5547 $m^2 \cdot g^{-1}$; however, it undergoes a significant reduction after two prolonged annealing treatments due to the potential collapse of its porous structure during the N-doping process.[34-37] Additionally, the nanopore of $NWSC_{0.6}$ may experience particle clogging, resulting in a decrease in its specific surface area.[38, 39] The high-specific-surface-area $NWSC_{0.6}$ carbon material possesses an abundant porous structure that facilitates the exposure of ORR active sites and enhances the mass transport of electrolytes/reactants, thereby enhancing its catalytic activity.[40, 41]

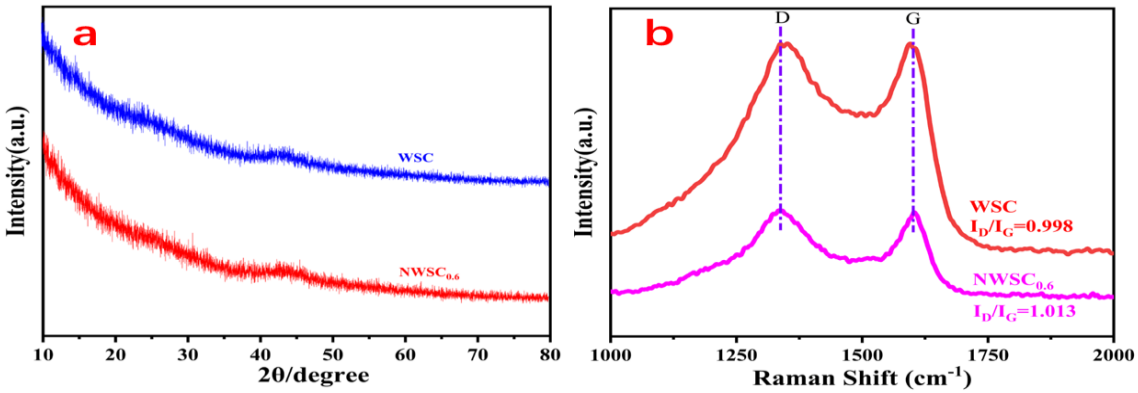

Fig. 2: (a) XRD patterns of the resultant WSC and $NWSC_{0.6}$, (b) Raman spectra of the different samples.

The surface microstructure and morphology of the $NWSC_{0.6}$ sample were examined using SEM to investigate the impact of carbonization temperature on pore structure, as depicted in Fig 3 (a, b). The final product exhibits an irregular shape, characterized by a relatively rough surface and prominent large pores. The carbon is activated by NaOH at 800 °C in an inert environment, resulting in a significant release of gas during the reaction between NaOH and carbon. The escape of gas leads to the formation of abundant pores and channels on the surface of $NWSC_{0.6}$, greatly increasing its surface area.[33] The presence of large pores in these structures facilitates the three-dimensional transport of materials, thereby promoting the entry of electrolyte, O_2, and its intermediates into the catalyst surface.[40, 42] This leads to enhanced reaction kinetics and improved catalytic activity. To further investigate the morphology of $NWSC_{0.6}$, TEM analysis (Fig 3c) and high-resolution transmission electron microscopy (HRTEM) measurements were conducted (Fig 3d). The TEM image reveals the complete carbon sheet, which is consistent with the SEM image findings. The HRTEM characterization further confirmed that the $NWSC_{0.6}$ sample exhibited an amorphous structure and a disordered carbon phase. The HAADF-STEM image of the $NWSC_{0.6}$ sample, depicted in Fig 3(e-h), reveals a homogeneous distribution of carbon (C), nitrogen (N), and oxygen (O) atoms, thereby confirming the successful incorporation of nitrogen dopants into the carbonaceous material. The elemental composition consists of 96.59% carbon (C), 1.14% nitrogen (N), and 2.28% oxygen (O). Furthermore, the incorporation of nitrogen atoms into the carbon skeleton enhances charge transfer due to the presence of highly defective carbons, thereby resulting in an increased activity for oxygen reduction reaction (ORR).[43]

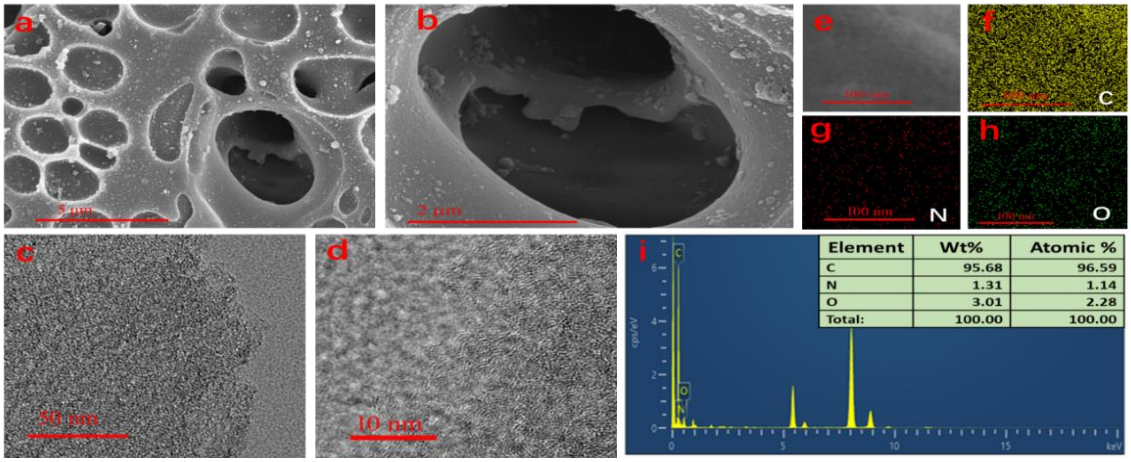

Fig. 3: (a, b) SEM, (c) TEM, (d) HR-TEM images, (e-h) elemental mapping images of $NWSC_{0.6}$ catalyst samples and (i) EDS pattern of $NWSC_{0.6}$ catalyst samples.

The composition and chemical state of elements in $NWSC_{0.6}$ samples were further determined through XPS investigation and analysis, revealing the coexistence of carbon, nitrogen, and oxygen (Fig 4a). In Fig 4 (b), the high-resolution C1s spectrum can be divided into three peaks, corresponding to the graphite structure (sp^2, C-C/C=C) at 284.6 eV, carbon-oxygen bonds in phenol, epoxy or hydroxyl groups at 285.9 eV with a possible contribution from C-N bonds, and carboxylic acids or esters at 289.5 eV.[18, 23, 44, 45] The presence of C-N/C-O bonds indicates the adsorption of N and O on the carbon material, thereby enhancing its electronic conductivity.[46] In the high-resolution O 1s spectrum shown in Fig 4(c), three distinct peaks at 531.4, 532.2, and 533.4 eV are observed, which can be attributed to C-O/C=O, C-OH/C-O-C, and-COOH functionalities, respectively.[45, 47] The presence of C-OH enhances the surface wettability, whereas the presence of -COOH induces additional defects and augments the number of active sites.[45] Fig 4(d) shows four typical N 1s peaks at energy levels of 406.5, 401.7, 400.1, and 398.3 eV, which correspond to oxidized N, graphite N, pyrrole N, and pyridine N respectively.[48] The active sites of ORR, namely Pyridine N and graphite N, are widely acknowledged for their ability to facilitate oxygen adsorption and selective oxygen reduction via the four-electron mechanism, thereby enhancing the performance of ORR.[19] The addition of Graphite N can effectively mitigate the inherent resistance of carbon materials and facilitate electron transfer within the carbon matrix.[49] The presence of electron donors in N-functional groups enables them to function as electroactive sites through ORR.[50] The presence of different nitrogen atoms can impact the charge density of the carbon structure, whereby the lone electron pair on pyrrole nitrogen can undergo conjugation with the double bond, functioning as an electron-donating group that enhances the electron cloud density around the carbon atom within the ring.[5, 23, 51]The pyridine nitrogen is non-conjugated, exhibiting higher electronegativity than carbon, resulting in electron density being localized on the pyridine nitrogen atoms.[34, 45, 52] This redistribution of charge further influences the adsorption mode of O_2, promoting its reduction.[15] In addition, the nitrogen atom provides a greater number of electrons compared to the carbon atom, thereby facilitating charge transfer and consequently reducing the dissociation barrier of the oxygen-oxygen bond.[24, 52] This ultimately enhances the catalytic efficiency of the ORR. When combined with the aforementioned findings, successful nitrogen doping into the carbon framework derived from walnut shell was achieved.

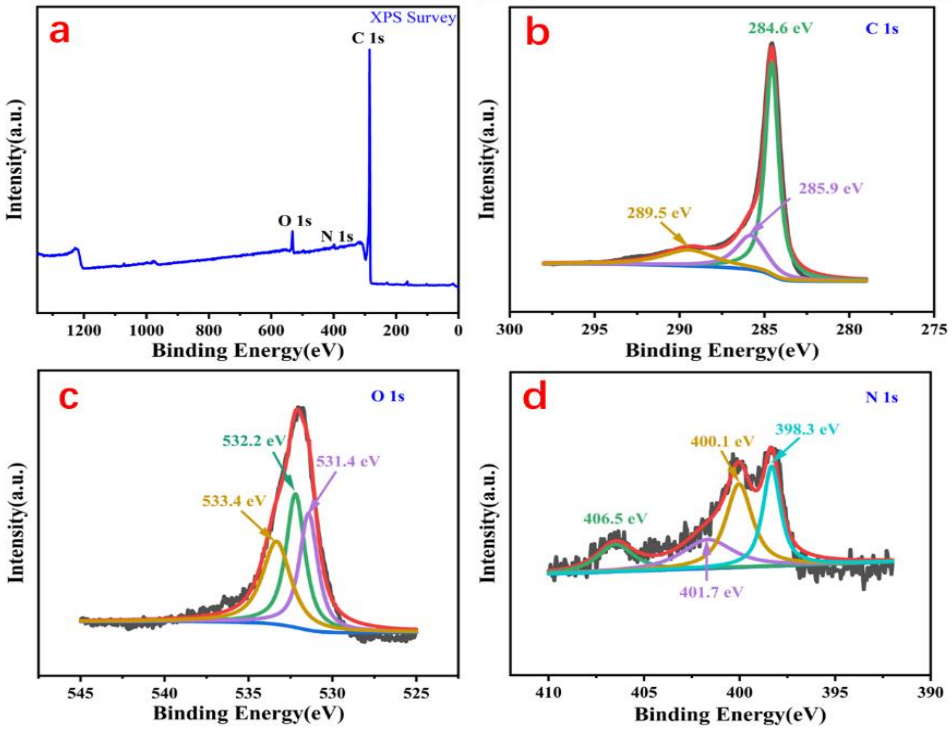

Fig. 4: XPS spectra of (a) XPS survey spectrum, (b) C 1s, (c) O 1s and (d) N 1s for $NWSC_{0.6}$ electrocatalyst.

Electrocatalytic performance

The ORR catalytic performance of WSC, $NWSC_{0.4}$, $NWSC_{0.5}$, $NWSC_{0.6}$, $NWSC_{0.7}$ and commercial Pt/C catalysts in aqueous solution saturated with O_2 at 0.1 M KOH was evaluated using Linear sweep voltammetry (LSV), as depicted in Fig 5a. $NWSC_{0.6}$ exhibited superior catalytic activity in terms of half-wave potential ($E_{1/2}$=0.849 V) compared to $NWSC_{0.7}$ ($E_{1/2}$= 0.733 V), $NWSC_{0.5}$ ($E_{1/2}$= 0.746 V), $NWSC_{0.4}$ ($E_{1/2}$=0.771 V), and WSC ($E_{1/2}$=0.679 V), as summarized in Table1. The $E_{1/2}$ of the $NWSC_{0.6}$ catalyst exhibited a positive shift of 9 mV compared to the commercial Pt/C catalyst ($E_{1/2}$=0.840 V). The enhanced ORR activity of $NWSC_{0.6}$ can be attributed to the disruption of electroneutrality in carbon nanosheets through nitrogen doping, resulting in active carbon atoms carrying a net positive charge that serve as electrocatalytic active centers. To further investigate the electrochemical ORR properties of these catalysts, we conducted CV measurements using rotating ring-disk electrode (RRDE) to elucidate their initial activity. In an O_2-saturated electrolyte solution containing 0.1 M KOH, all catalysts exhibited distinct cathodic peaks corresponding to oxygen reduction at potentials ranging from 0.7V to 0.9V (Fig S2). Notably, the peak potential of the $NWSC_{0.6}$ catalyst was significantly higher than that of the other catalysts, indicating superior ORR activity. The observed activity trend in the CV curves is consistent with that observed in LSV curves. The XPS analysis reveals a significant presence of pyridine and graphitic nitrogen, which greatly facilitates the ORR process. Furthermore, in addition to the advantages provided by nitrogen-induced active sites and high electrical conductivity, the defect nature of $NWSC_{0.6}$ also generates defect-induced active sites that synergistically promote the enhancement of ORR activity. This is evidenced by the high I_D/I_G ratio observed in Raman spectra. Finally, $NWSC_{0.6}$ exhibits a porous structure and possesses a significantly high surface area of 2636.5547 $m^2 \cdot g^{-1}$. This unique porous architecture and expansive surface area not only facilitate the generation of abundant active sites, effectively exposing the catalytic center, but also greatly enhance the efficiency of oxygen and electrolyte mass transport processes.

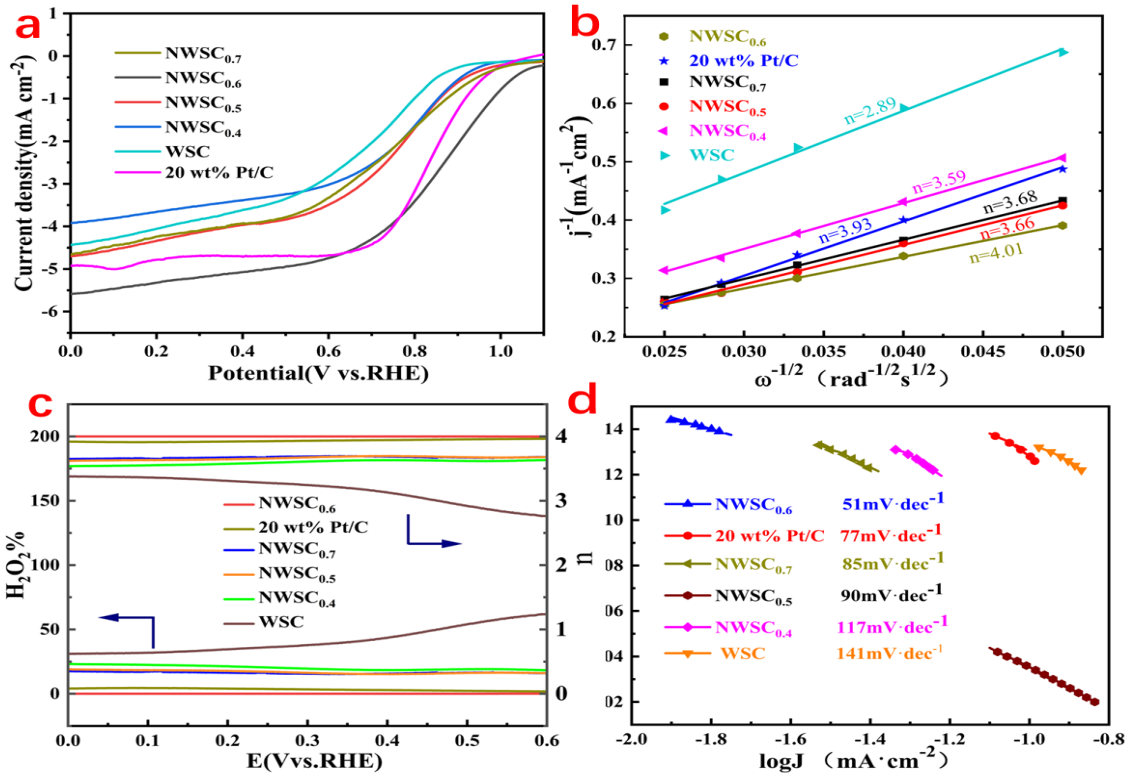

Fig 5: (a) ORR polarization curves for different catalysts at 1600 rpm, (b) Koutecky-Levich plots of different catalysts at different potentials, (c) The electron transfer number and percentage of peroxide of different catalysts at different potentials, (d) Tafel plots of different catalysts deriving from the LSVs data.

Table-1: The electrochemical performance of the different sample under the same test conditions.

Sample	Half-wave potential ($E_{1/2}$, V)	The electron transfer number (n)	The average H_2O_2 yield	The Tafel slope ($mV \cdot dec^{-1}$)
WSC	0.679	2.95	49.4%	141
$NWSC_{0.4}$	0.771	3.62	19.7%	117
$NWSC_{0.5}$	0.746	3.68	16.8%	90
$NWSC_{0.6}$	0.849	3.99	<1%	51
$NWSC_{0.7}$	0.733	3.69	15.7%	85
commercial Pt/C	0.840	3.94	<1%	77

To further elucidate the electron transfer mechanism, LSV curves at various rotation rates are presented in Fig 5b, and ESI, S3-S8. The corresponding Koutecky-Levich (K-L) diagram substantiates a highly linear correlation between J^{-1} and $\omega^{-1/2}$, thereby indicating the first-order reaction kinetics of ORR. Within the potential range of 0.2 V to 0.7 V, the electron transfer number (n) for WSC, $NWSC_{0.4}$, $NWSC_{0.5}$, $NWSC_{0.6}$, $NWSC_{0.7}$ and the commercial Pt/C catalysts is approximately 2.89, 3.59, 3.66, 4.01, 3.68 and 3.93 respectively. The results demonstrate that $NWSC_{0.6}$ exhibits a four-electron pathway for oxygen reduction, making it an effective air cathode catalyst for facilitating the 4-electron transfer mechanism. To further showcase their high activity, RRDE technology was employed to calculate the H_2O_2 yield of these catalysts. The average H_2O_2 yield of $NWSC_{0.6}$ was found to be less than 1%, which is lower compared to WSC (49.4%), $NWSC_{0.4}$ (19.7%), $NWSC_{0.5}$ (16.8%), and $NWSC_{0.7}$ (15.7%). These findings indicate that the reduction of O_2 by $NWSC_{0.6}$ occurs through a four-electron transfer step, enabling ORR to directly convert O_2 into H_2O with excellent selectivity (Fig 5c). The electron transfer numbers (n) of WSC, $NWSC_{0.4}$, $NWSC_{0.5}$, $NWSC_{0.6}$, $NWSC_{0.7}$, and commercial Pt/C catalysts are approximately 2.95, 3.62, 3.68, 3.99, 3.69 and 3.94, respectively, as summarized in Table1. The electrochemical active surface area (ECSA) of the ORR catalysts was determined by calculating the double-layer capacitance (C_{dl}) from cyclic voltammetry (CV) curves obtained at various scanning rates in a N_2-saturated 0.1 M KOH solution, as illustrated in ESI (Fig S9). The ECSA value of $NWSC_{0.6}$ was 43.43 $m^2 \cdot g^{-1}$, surpassing the values of WSC (19.18$m^2 \cdot g^{-1}$) and commercial Pt/C (35.56 $m^2 \cdot g^{-1}$). The $NWSC_{0.6}$ demonstrates a higher electrochemically active surface area, while the catalytic material exhibits comparable or superior electrocatalytic properties, thus showcasing its immense potential for diverse applications and effectively enhancing catalytic performance through increased exposure of active sites. The $NWSC_{0.6}$ possesses a suitable porous structure and exhibits remarkable ORR properties, which can effectively facilitate the transportation of O_2 and electrolytes. The Tafel curve (Fig 5d) demonstrates that the Tafel slope of $NWSC_{0.6}$ is measured at a lower value of 51$mV \cdot dec^{-1}$ compared to the reference value for a Pt/C catalyst with a loading of 20 wt% (77 $mV \cdot dec^{-1}$), as well as being lower than that observed for $NWSC_{0.7}$ (85 $mV \cdot dec^{-1}$). Furthermore, it is also noted that the Tafel slopes for $NWSC_{0.5}$ (90 $mV \cdot dec^{-1}$), $NWSC_{0.4}$ (117$mV \cdot dec^{-1}$), and WSC (141 $mV \cdot dec^{-1}$) are higher than those recorded for the aforementioned samples. The samples labeled $NWSC_{0.6}$ exhibited superior kinetics in terms of ORR compared to the other tested materials. The stability factor plays a crucial role in influencing the ORR of fuel cells. As depicted in Fig S10, the accelerated durability test conducted after 2000 CV cycles reveals that the ORR activity of the $NWSC_{0.6}$ catalyst only diminishes by 9 mV, whereas that of the 20 wt% Pt/C catalyst attenuates by 11 mV. This observation further confirms that the $NWSC_{0.6}$ catalyst exhibits superior durability compared to its counterpart. Consequently, it can be inferred that $NWSC_{0.6}$ holds promising potential as an ORR electrocatalyst for practical applications in fuel cells.

The K-L analysis confirmed that the ORR process of the synthesized metal-free nitrogen-permeable carbon skeleton $NWSC_{0.6}$ catalyst followed a four-electron pathway instead of a two-electron pathway, with an approximate n value of 3.99. The performance of the $NWSC_{0.6}$ catalyst surpasses that of the WSC catalyst. The reasonable design of porous carbon in walnut shell as an electrocatalyst was achieved by incorporating urea dopant, thereby enhancing its ORR catalytic activity, given the nitrogen deficiency in most low-cost renewable energy sources.[53] The presence of graphite N and pyridine N in $NWSC_{0.6}$ results in the electronegativity of the nitrogen atom, rendering the adjacent C atom electron-deficient and potentially facilitating the generation of a positive charge on this neighboring carbon atom.[23] The positively charged site facilitates the adsorption of O_2 and promotes the breaking of O-O bonds, leading to the complete reduction of O_2 to H_2O through a 4-electron pathway.[14, 31] In an aqueous electrolyte, the cathode reaction process of oxygen reduction in a fuel cell proceeds through the following steps: initial diffusion and adsorption of oxygen molecules onto the electrocatalyst surface, then transfer of electrons from the anode to the oxygen molecules, subsequent breaking of the O=O bond, and eventual release of

resulting OH^- ions into the solution.[5, 23] The reaction of the direct four-electron pathway in alkaline electrolytes proceeds as follows:[23]

$$O_2 + H_2O + 2e^- \rightarrow OOH^- + OH^- \quad (1)$$
$$H_2O + OOH^- + 2e^- \rightarrow 3OH^- \quad (2)$$
$$O_2 + 2H_2O + 4e^- \rightarrow 4OH^- \quad (3)$$

Therefore, our synthesized material demonstrates exceptional catalytic properties for ORR, and the superior catalytic activity of $NWSC_{0.6}$ can be attributed to two key factors. The abundant large-pore carbon skeleton enhances electron transport efficiency and exposes a multitude of active sites, thereby facilitating reaction acceleration. On the contrary, the incorporation of nitrogen leads to the regulation of functional groups (pyridine nitrogen and graphite N) on the surface of the carbon matrix, thereby enhancing catalytic activity for ORR. The presence of a sufficiently high electrochemically active surface area facilitates the exposure of more active sites for catalytic services and enhances efficient mass transport.

Catalytic performance for Mg-air battery

To validate the exceptional ORR activity of $NWSC_{0.6}$, we conducted a cathode catalyst test on $NWSC_{0.6}$ in a magnesium-air cell at a current density of 5 $mA \cdot cm^{-2}$. These experimental findings align consistently with the kinetics of oxygen reduction in an alkaline environment (Fig 6a). The $NWSC_{0.6}$ catalyst was utilized as the air cathode in the magnesium-air battery, while a magnesium alloy plate served as the anode and a 3.5% salt water solution functioned as the electrolyte. The $NWSC_{0.6}$-based Mg-air battery exhibits a consistent discharge voltage profile, with an initial discharge voltage of approximately 1.25 V, maintaining stability at 1.23 V even after 45 hours of continuous discharge, and eventually settling at 1.19 V after 60 hours. The Pt/C-based Mg-air battery exhibits an initial discharge voltage of 1.22 V, consistently lower than that of the $NWSC_{0.6}$-based Mg-air battery throughout the entire discharge process, until reaching a discharge voltage of 1.15 V after 60 hours. The polarization curve and power density diagram of the neutral magnesium air battery are depicted in Fig 6b. $NWSC_{0.6}$ exhibits a higher power density of 65.6$mW \cdot cm^{-2}$ compared to 20% Pt/C (62.5 $mW \cdot cm^{-2}$). As the current density increases, both $NWSC_{0.6}$ and 20% wt% Pt/C experience a decrease in battery voltage. It is noteworthy that at the same current density, $NWSC_{0.6}$ surpasses the voltage of 20% Pt/C. The results further confirm the excellent catalytic activity and durability of the $NWSC_{0.6}$-based Mg-air battery, thereby demonstrating its superior ORR catalytic performance in seawater battery applications.

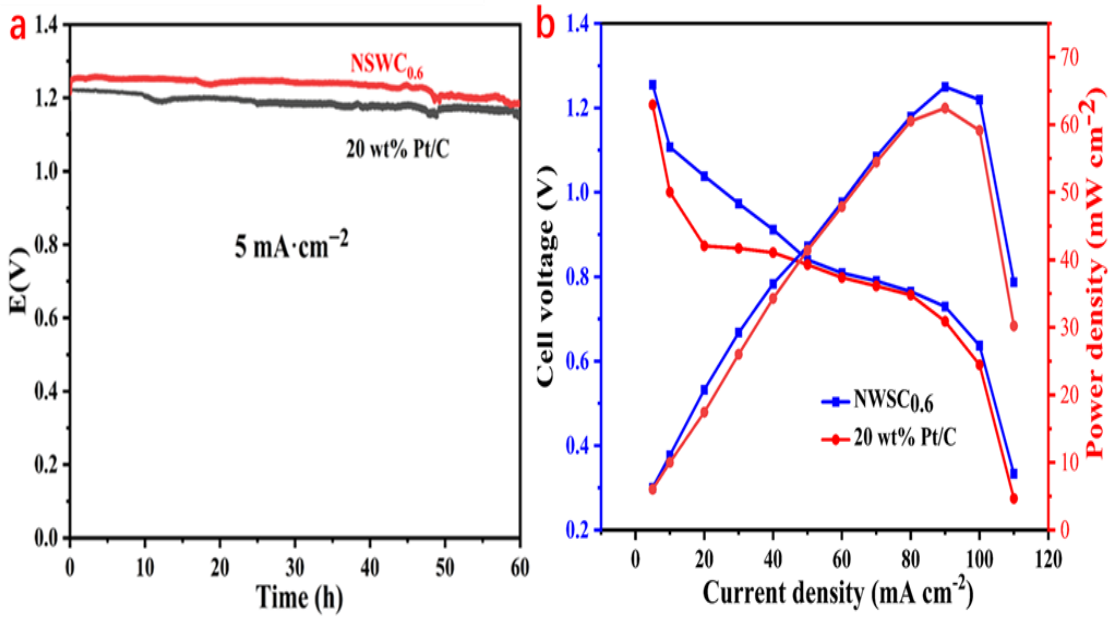

Fig. 6: Full-cell test of catalysts. (a) Discharge profiles of $NWSC_{0.6}$ electrocatalyst and 20 wt% Pt/C at 5 $mA \cdot cm^{-2}$ in Mg-air batteries. (b) Polarization curves and power density plots of the Mg-air batteries with $NWSC_{0.6}$ electrocatalyst and 20 wt% Pt/C as the cathode catalysts.

Conclusions

A series of nitrogen-doped biomass carbon materials were prepared by adjusting the doping ratio, using walnut shell as a carbon source, NaOH as an activator, and urea as a nitrogen source. The optimal product ($NWSC_{0.6}$) exhibiting outstanding cathodic oxygen reduction performance was synthesized through the addition of urea, in a mass ratio of 1:6 with pre-carbonized carbon to NaOH at 800℃ for a duration of 3 hours following pyrolysis. The introduction of a nitrogen source resulted in the modification of the chemical structure of the material, leading to an increase in defects within the carbon material and ultimately enhancing the catalytic activity of the carbon catalyst. The electrochemical test results also demonstrate that the N-doped porous carbon exhibits enhanced catalytic activity for oxygen reduction compared to the WSC. Consequently, this study presents a novel approach to fabricate defect sites and optimize the structure of carbon catalysts, thereby offering promising prospects for their application in fuel cells and metal-air batteries.

Conflicts of interest

Author Kun Liu has received the Key Project of Education Department from Anhui Province and the Scientific Research Foundation for High-Level Talents from West Anhui University. Author Xucheng Fu has received the Excellent Research and Innovation Team Project from Anhui Province. The authors declare that they have no known competing financial interests or personal relationships that could have appeared to influence the work reported in this paper.

Acknowledgements

This work was financially supported by the Excellent Research and Innovation Team Project of Anhui Province(2023AH010077), the Key Project of Education Department of Anhui Province (2022AH051679), the Scientific Research Foundation for High-Level Talents of West Anhui University (WGKQ202001001), the Residual Funds from Longitudinal Research Projects (0041025025), the Key Project of Education Department of Anhui Province (2025AHGXZK30343). We would like to express our sincere gratitude to the Key Laboratory of Conservation and Utilization of Characteristic Biological Resources of Dabie Mountain in Anhui Province for generously providing us with all the necessary experimental facilities.

Funding

The expenses for these achievements were fully supported by the key project of the Natural Science Fund of Anhui Provincial Department of Education (2022AH051679), the project of Anhui Provincial Excellent Scientific Research Team (2023AH010077), the High-level Talents Initiation Project of West Anhui University (WGKQ202001001), and the Residual Funds from Longitudinal Research Projects (0041025025), the Key Project of Education Department of Anhui Province (2025AHGXZK30343).

References

1. S. Niu, S. Li, and Y. Du, , et al, How to Reliably Report the Overpotential of an Electrocatalyst, *ACS Energy Letters*, **5**,4 (2020).
2. T. Asefa, C. Tang, M. Ramirez-Hernandez, Nanostructured Carbon Electrocatalysts for Energy Conversions, *Small*, **17**,48 (2021).
3. P. Kallem, N. Yanar, H. Choi, Nanofiber-Based Proton Exchange Membranes: Development of Aligned Electrospun Nanofibers for Polymer Electrolyte Fuel Cell Applications, *ACS Sustainable Chemistry & Engineering*, **7**,2 (2018).
4. Y. Wang, F. Chu, and J. Zeng, et al, Single Atom Catalysts for Fuel Cells and Rechargeable Batteries: Principles, Advances, and Opportunities, *ACS Nano*, **15**,1 (2021).
5. P. Kaur, G. Verma, S.S. Sekhon, Biomass derived hierarchical porous carbon materials as oxygen reduction reaction electrocatalysts in fuel cells, *Progress in Materials Science*, **102**, 1(2019).
6. D. G. Wang, T. Qiu, and W. Guo, et al, Covalent organic framework-based materials for energy applications, *Energy & Environmental Science*, **14**,2 (2021).
7. Q. Dong, H. Wang, and S. Ji, et al, Mn Nanoparticles Encapsulated within Mesoporous Helical N-Doped Carbon Nanotubes as Highly Active Air Cathode for Zinc-Air Batteries, *Advanced Sustainable Systems*, **3**,12 (2019).
8. G. Yang, C. Erbay, and S. I. Yi, et al, Bifunctional nano-sponges serving as non-precious metal catalysts and self-standing cathodes for high performance fuel cell applications, *Nano Energy*, **22**, 3(2016).
9. C. Du, X. Gao, W. Chen, Recent developments in copper-based, non-noble metal electrocatalysts for the oxygen reduction reaction, *Chinese Journal of Catalysis*, **37**,7 (2016).
10. S.T. Zhang, Y. Meng, and P.X. Hou, et al, Multiscale nanoengineering fabrication of air electrode catalysts in rechargeable Zn-air batteries, *J Colloid Interface Sci*, **664**, 9 (2024).
11. J. Cai, X. Zhang, and Y. Zhang, et al, Titania nanotubes coated with graphene as a promising

catalyst for the oxygen reduction reaction, *New Journal of Chemistr*y, **44**,18 (2020).
12. Y. Chang, J. Li, and T. Zhang, et al, Correlating oxygen reduction activity of N, S-co-doped carbon with the structures of dopant molecules, *Journal of Alloys and Compounds*, **986**,5(2024).
13. Z. Li, S. Ji, and H. Liu, et al, Constructing Asymmetrical Coordination Microenvironment with Phosphorus-Incorporated Nitrogen-Doped Carbon to Boost Bifunctional Oxygen Electrocatalytic Activity, *Advanced Functional Materials*, **34**,18 (2024).
14. F. Zhang, H. Wang, Pyridinic N and semi-ionic F Co-functionalized biochar nanofibers as efficient metal-free electrocatalysts for oxygen reduction reaction, *Journal of Materials Science*, **59**,8(2024).
15. Y. Fu, C. Cao, and W. Song, et al, Self-Assembly Strategy for Constructing Porous Boron and Nitrogen Co-Doped Carbon as an Efficient ORR Electrocatalyst toward Zinc-Air Battery, *Chemistry- A European Journal*, **30**,28 (2024).
16. L. Yan, Y. Liu, and J. Hou, et al, High-Efficiency Oxygen Reduction Reaction Revived from Walnut Shell, *Molecules*, **28**,5 (2023).
17. S. Fordos, N. Abid, and M. Gulzar, et al, Recent development in the application of walnut processing by-products (walnut shell and walnut husk), *Biomass Conversion and Biorefinery*, **13**,16 (2023).
18. Y. Bao, H. Xu, and P. Chen, et al, Redox molecule Alizarin red S anchored on biomass-derived porous carbon for enhanced supercapacitive performance, *New Journal of Chemistry*, **46**,30 (2022).
19. M. Hao, R. Dun, and Y. Su, et al, In situ self-doped biomass-derived porous carbon as an excellent oxygen reduction electrocatalyst for fuel cells and metal–air batteries, *Journal of Materials Chemistry A*, **9**, 25 (2021).
20. L. Song, J. Chang, and Y. Ma, et al, Biomass-derived nitrogen and sulfur co-doped carbon microtubes for the oxygen reduction reaction, *Materials Chemistry Frontiers*, **4**,11 (2020).
21. K. Zhang, Z. Zhang, and H. Shen, et al, Electronic modulation of Ni_2P through anion and cation substitution toward highly efficient oxygen evolution, *Science China Materials*, **65**,6 (2022).
22. S. Li, Z. Zhuang, and L. Xia, et al, Improving the electrophilicity of nitrogen on nitrogen-doped carbon triggers oxygen reduction by introducing covalent vanadium nitride, *Science China Materials*, **66**,1 (2022).
23. M. Jalalah, H. Han, and A.K. Nayak, et al, Biomass-derived metal-free porous carbon electrocatalyst for efficient oxygen reduction reactions, *Journal of the Taiwan Institute of Chemical Engineers*, **147**,6 (2023).
24. Y. Wu, A. Muthukrishnan, and S. Nagata, et al, Kinetic Understanding of the Reduction of Oxygen to Hydrogen Peroxide over an N-Doped Carbon Electrocatalyst, *The Journal of Physical Chemistry C*, **123**,7 (2019).
25. K. Liu, K. Hu, and N. N. Zhang, et al, Design of Fe and Cu bimetallic integration into nitrogen-containing microporous graphene-like carbon via a hard-template-assisted strategy as an oxygen reduction catalyst for Al-air batteries, *New Journal of Chemistry*, 48, 27(2024).
26. K. Liu, Y. J. Ling, and X. L. Guan, et al, Design of Fe/Co-N doped porous carbon sheets using a hard template strategy as an oxygen reduction catalyst for Mg-air batteries, *New Journal of Chemistry*, 48, 33(2024).
27. R. Liu, H. Zhang, and S. Liu, et al, Shrimp-shell derived carbon nanodots as carbon and nitrogen sources to fabricate three-dimensional N-doped porous carbon electrocatalysts for the oxygen reduction reaction, *Physical Chemistry Chemical Physics*, **18**,5 (2016).
28. J. H. Park, J. H. Shin, and J. M. Ju, et al, Modulating the electrocatalytic activity of N-doped carbon frameworks via coupling with dual metals for Zn-air batteries, *Nano Converg*, **9**,1 (2022).
29. L. Lu, J. Yu, and Z. Wu, et al, Shaddock peel derived nitrogen and phosphorus dual-doped hierarchical porous carbons as high-performance catalysts for oxygen reduction reaction, *International Journal of Hydrogen Energy*, **44**, 49 (2019).
30. G. Kumar, S.K. Das, and E.E. Siddharthan, et al, An interfacially stacked covalent porous polymer on graphene favors electronic mobility: ensuring accelerated oxygen reduction reaction kinetics by an in situ study, *Journal of Materials Chemistry A*, **11**, 35 (2023).
31. V. Priya K, M. Thomas, and R. Illathvalappil, et al, Template assisted synthesis of Ni,N co-doped porous carbon from Ni incorporated ZIF-8 frameworks for electrocatalytic oxygen reduction reaction, *New Journal of Chemistry*, **44**,28 (2020).
32. X. Zhang, P. Yu, and G. Xing, et al, Iron Single Atoms-Assisted Cobalt Nitride Nanoparticles to Strengthen the Cycle Life of Rechargeable Zn-Air Battery, *Small*, **18**, 51 (2022).
33. Y. Hou, F. Ma, and Z. Fu, et al, Encapsulation of stearic-palmitic acid in alkali-activated coconut shell and corn cob biochar to optimize energy storage, *Journal of Energy Storage*, **66**, 9 (2023).
34. H. Liu, H. Liu, and S. Di, et al, Advantageous Tubular Structure of Biomass-Derived Carbon for

High-Performance Sodium Storage, *ACS Applied Energy Materials*, **4**, 5 (2021).

35. Z. Wu, J. Zhang, and S. Hu, et al, Efficiently treating waste nylon-tire to prepare sulfur and nitrogen doped porous carbon material via pyrolysis and activation, *Journal of Environmental Chemical Engineering*, **10**,4 (2022).
36. F. Zhao, F. Song, Q. Chen, Nitrogen/sulfur codoped FCC-slurry-based porous carbon materials in symmetric supercapacitors, *Applied Surface Science*, **561**,2 (2021).
37. F. Zaman, M.W. Ishaq, and A. Munawar, et al, Aesculus indica-derived heteroatom-doped carbon as an electrode material for super-capacitor, *Carbon Letters*, **33**,7 (2023).
38. B. K. Kim, G. H. Gwak, and T. Okada, et al, Effect of particle size and local disorder on specific surface area of layered double hydroxides upon calcination-reconstruction, *Journal of Solid State Chemistry*, **263**,9 (2018).
39. E. Moretti, A.I. Molina, and G. Sponchia, et al, Low-temperature carbon monoxide oxidation over zirconia-supported $CuO–CeO_2$ catalysts: Effect of zirconia support properties, *Applied Surface Science*, **403**,6 (2017).
40. L. Dai, C. Feng, and Y. Luo, et al, CoFe Alloys Dispersed on Se, N Co-Doped Graphitic Carbon as Efficient Bifunctional Catalysts for Zn-Air Batteries, *Chemistry-A European Journal*, **30**,2 (2024).
41. D. Bi, N. Shen, and Z. Tang, et al, Defective Carbon Derived Using a Dissolution-Recrystallization Strategy for Oxygen Reduction Electrocatalysis, *ACS Appl Mater Interfaces*, **15**, 25 (2023).
42. S. Kang, S. Li, and X. Xiao, et al, Porous MCo_2O_4(M = Zn, Cu, Fe, Mn) as high efficient bi-functional catalysts for oxygen reduction and oxygen evolution reaction, *Nanotechnology*, **33**, 45 (2022).
43. B. Jing, S. You, and Y. Ma, et al, Fe_3Se_4/FeSe heterojunctions in cornstalk-derived N-doped carbon framework enhance charge transfer and cathodic oxygen reduction reaction to boost bio-electricity generation, *Applied Catalysis B: Environmental*, **244**,11(2019).
44. F. Pan, Z. Cao, and Q. Zhao, et al, Nitrogen-doped porous carbon nanosheets made from biomass as highly active electrocatalyst for oxygen reduction reaction, *Journal of Power Sources*, **272**, 9 (2014).
45. J. Yang, W. Liu, and Y. Sun, et al, Improved oxygen reduction activity on biomass derived carbon catalysts via microbial fermentation pre-treatment and oxygen etching, *Fuel Processing Technology*, **248**,10 (2023).
46. X. Gao, H. Zhao, and S. Zhang, et al, Mechanochemical Modification of Oxygen/Nitrogen Species on Surface of Hard Carbon for Improved Sodium Storage, *ACS Sustainable Chemistry & Engineering*, **10**,1 (2021).
47. D. M. Fernandes, A. S. Mestre, and A. Martins, et al, Biomass-derived nanoporous carbons as electrocatalysts for oxygen reduction reaction, *Catalysis Today*, **357**,12 (2020).
48. S. Ren, X. Qu, and X. Zhang, et al, Valorization of biomass furfural residue: Nitrogen-doped porous carbon towards electrocatalytic reaction, *Industrial Crops and Products*, **193**,12 (2023).
49. M. Huang, S. Liu, and S. Gong, et al, Silver Nanoparticles Encapsulated in an N-Doped Porous Carbon Matrix as High-Active Catalysts toward Oxygen Reduction Reaction via Electron Transfer to Outer Graphene Shells, *ACS Sustainable Chemistry & Engineering*, **7**,19 (2019).
50. K. Maliutina, J. Huang, and T. Su, et al, Biomass-derived Ta,N,S co-doped CNTs enriched carbon catalyst for efficient electrochemical oxygen reduction, *Journal of Alloys and Compounds*, **888**, 9 (2021).
51. H. Xu, Y. Bao, and S. Zuo, et al, Enhanced Electrochemical Performance of Biomass Porous Carbon Adsorption Congo Red, *Journal of The Electrochemical Society*, **169**,1(2022).
52. N. Xue, J. Liu, and P. Wang, et al, Scalable synthesis of $Fe_{(3)}N$ nanoparticles within N-doped carbon frameworks as efficient electrocatalysts for oxygen reduction reaction, *J Colloid Interface Sci*, **580**,6(2020).
53. Q. Li, Y. N. Zhang, and S. Feng, et al, N, S self-doped porous carbon with enlarged interlayer distance as anode for high performance sodium ion batteries, *International Journal of Energy Research*, **45**, 5 (2020).